Analysis of a transmission mode scanning microwave microscope for subsurface imaging at the nanoscale

A. O. Oladipo, A. Lucibello, M. Kasper, S. Lavdas, G. M. Sardi, E. Proietti, F. Kienberger, R. Marcelli, and N. C. Panoiu

Articles you may be interested in

Gallium nitride nanowire probe for near-field scanning microwave microscopy
Appl. Phys. Lett. **104**, 023113 (2014); 10.1063/1.4861862

Scanning microwave microscopy/spectroscopy on metal-oxide-semiconductor systems
J. Appl. Phys. **108**, 064315 (2010); 10.1063/1.3482065

Invited Review Article: Microwave spectroscopy based on scanning thermal microscopy: Resolution in the nanometer range
Rev. Sci. Instrum. **79**, 041101 (2008); 10.1063/1.2908445

Parallel-detection microwave spectroscopy system for breast imaging
Rev. Sci. Instrum. **75**, 2305 (2004); 10.1063/1.1764609

Quantitative microwave evanescent microscopy of dielectric thin films using a recursive image charge approach
Appl. Phys. Lett. **84**, 4647 (2004); 10.1063/1.1759389

Analysis of a transmission mode scanning microwave microscope for subsurface imaging at the nanoscale

A. O. Oladipo,[1,2,a)] A. Lucibello,[3] M. Kasper,[4] S. Lavdas,[2] G. M. Sardi,[3] E. Proietti,[3] F. Kienberger,[5] R. Marcelli,[3] and N. C. Panoiu[2]

[1]Bio-Nano Consulting, The Gridiron Building, One Pancras Square, N1C 4AG London, United Kingdom
[2]Electronic and Electrical Engineering Department, University College London, Torrington Place, WC1E 7JE London, United Kingdom
[3]National Research Council, Institute for Microelectronics and Microsystems, via del Fosso del Cavaliere 100, 00133 Rome, Italy
[4]Biophysics Institute, Johannes Kepler University Linz, Gruberstrasse 40, 4020 Linz, Austria
[5]Keysight Technologies Austria GmbH, Gruberstrasse 40, 4020 Linz, Austria

We present a comprehensive analysis of the imaging characteristics of a scanning microwave microscopy (SMM) system operated in the transmission mode. In particular, we use rigorous three-dimensional finite-element simulations to investigate the effect of varying the permittivity and depth of sub-surface constituents of samples, on the scattering parameters of probes made of a metallic nano-tip attached to a cantilever. Our results prove that one can achieve enhanced imaging sensitivity in the transmission mode SMM (TM-SMM) configuration, from twofold to as much as $5\times$ increase, as compared to that attainable in the widely used reflection mode SMM operation. In addition, we demonstrate that the phase of the S_{21}-parameter is much more sensitive to changes of the system parameters as compared to its magnitude, the scattering parameters being affected the most by variations in the conductivity of the substrate. Our analysis is validated by a good qualitative agreement between our modeling results and experimental data. These results suggest that TM-SMM systems can be used as highly efficient imaging tools with new functionalities, findings which could have important implications to the development of improved experimental imaging techniques. © 2014 AIP Publishing LLC. [http://dx.doi.org/10.1063/1.4897278]

Imaging at the nanoscale is becoming a major underlying driving force behind many key advancements in biology,[1,2] medicine,[3] materials science,[4,5] electronics,[6,7] and other fields of science and technology. Several imaging techniques have been employed to observe, characterize, and/or control nanoscale phenomena in materials and devices. Some of such broadly used techniques that allow one to accurately retrieve at the nanoscale the local structural, topographic, and dielectric properties of materials include the atomic force microscopy (AFM),[8,9] the electrostatic force microscopy (EFM),[10,11] and the scanning microwave microscopy (SMM).[12,13]

The SMM technique has been widely used in materials science and semiconductor industry, e.g., for calibrated capacitance measurements and dopant profiling. SMM uniquely combines the speed, versatility, and accuracy of the well-established performance network analyser (PNA) with the high sensitivity of the AFM technique.[14,15] In state-of-the-art SMM systems, a continuous microwave signal (typically 1 GHz to 20 GHz) generated by the PNA is propagated to a conductive AFM probe consisting of a cantilever, cone, and spherical tip, where the electromagnetic signal is partly reflected and partly transmitted. The specific ratio between these two components depends on the impedance experienced by the signal at the tip-sample interface. The PNA measures the ratio between the reflected and outgoing signals, defined as the S_{11} parameter. This reflection

mode SMM (RM-SMM) is now well established, with advanced probe designs, calibration algorithms, and fully integrated hardware and software systems being commonly used. However, subsurface characterization via RM-SMM is limited to depths of $\sim$500 nm, as structural constituents located beyond this depth no longer affect the reflected signal in a measurable way. By contrast, the transmitted signal interacts with such subsurface scatterers irrespective of the depth at which they are located, hence the transmission mode SMM (TM-SMM) can give more detailed (subsurface) images of samples than can be obtained in RM-SMM. Unlike other transmission techniques like the transmission electron microscope, the low energy microwave used in TM-SMM do not damage (biological) samples. Guided by these ideas, in this letter, we provide the first analysis of a SMM system operated in the transmission mode and prove that it allows one to achieve significantly improved subsurface analysis of samples as compared to RM-SMM, chiefly due to increased sensitivity of the transmission S-parameter, S_{21}.

In our analysis, we used three-dimensional (3D) finite-element method (FEM) to characterize the TM-SMM system. For the sake of clarity, we stress that sensitivity improvement refers to larger S-parameter variation for the same change in specific sample properties. Because 3D FEM provides insights into the electromagnetic interaction between the probe and sample that are not accessible via commonly used experimental techniques, it has become a powerful tool in guiding the experimental work, calibration of imaging systems, and interpretation and validation of

a)Abiola.Oladipo@bio-nano-consulting.com

experimental findings. In our study, we determined the 3D electric field distribution of the TM-SMM system and investigated the effect of varying the conductivity of the (silicon) substrate and the depth of subsurface constituents of sample on the S-parameters and their frequency dependence. We also varied the permittivity of buried constituents of samples while keeping the permittivity of the cover material constant and vice versa and studied the effect of these variations on the S-parameters. Finally, we compared our findings with experimental results.

The TM-SMM system shown schematically in Fig. 1(a) is a complementary design to the RM-SMM (PNA and AFM-tip) configuration, with the integration of a new controllable (along x, y, and z axes) sample holder and a SMA-type probe. In this technique, the microwave signal from the PNA port 1 propagates to the SMA-type probe, which acts as a radiating antenna, and through the sample to be recorded by the AFM-type probe at the other side of the sample. In this case, the AFM-type probe is the monitoring/sensing probe, which determines the lateral resolution of the TM-SMM for imaging purpose. As in the RM-SMM, part of the incoming signal is reflected back to the excitation port 1 and the PNA measures the ratios of the transmitted (forward) and reflected (backward) signals to the incoming signal as S-parameters $S_{21} = \rho_{21}e^{i\varphi_{21}}$ and $S_{22} = \rho_{22}e^{i\varphi_{22}}$, respectively. Here, ρ_{22}, ρ_{21} ($\varphi_{22}, \varphi_{21}$) are the amplitudes (phases) of the S-parameters. Note that unlike the RM-SMM case, in the TM-SMM the cantilever is located at port 2 of the PNA (see Fig. 1). The measured S-parameters depend on the impedance seen from the ports of the PNA, which in turn is determined by the electrical properties of the sample.

The sample presented in Fig. 1 comprises a relatively thick layer of silicon substrate ($h_{Si} = 500 \, \mu m$) with varying levels of dopant concentration along its cross-section, the sample conductivity, σ_s, varying from 0.3 S/m to 3000 S/m. The topographic image shown in Fig. 1(b) suggests that the sample is approximately flat, with maximum variation of 0.22 nm. In the absence of any topographic cross-talk, we obtained the S-parameter amplitude and phase contrast images shown in Figs. 1(c) and 1(d), respectively. These images clearly show sample regions with different dopant concentration (SMM from Agilent Technologies, Chandler, USA).

In order to analyze the electromagnetic interactions between the probe and sample and determine the system sensitivity to variations of key parameters, we performed 3D FEM simulations of the TM-SMM system by using EMPro, a commercially available software.[16] Our 3D FEM model, shown in Fig. 2(a), includes the complete AFM-type probe (cantilever, cone, and spherically shaped tip, $r_{tip} = 100$ nm), in contact to the sample at one end and at the other end separated from a SMA-type probe by a distance, $d = 250 \, \mu m$. Our FEM model assumes that port 1 is the excitation port.

Figure 2(b) plots the normalized electric field distribution in the TM-SMM system. It shows a field pattern emerging from the SMA-type probe and radiating towards the sample. On the other side of the sample, the field is strongly localized around the AFM-type probe, the largest field amplitude being around the tip. The field profile nearby the lateral sides of the sample suggests that the path of the waves traveling between the two ports does not go entirely through the sample, so that a calibration approach is necessary to isolate the electromagnetic interactions at the tip from the parasitic contributions from the other parts of the system. Figure 2(c) shows the relative electric field amplitude within the various layers of the sample. The field profiles presented in Fig. 2 also underline the importance of using a 3D computational analysis of the TM-SMM system, as the geometry does not have axial symmetry.
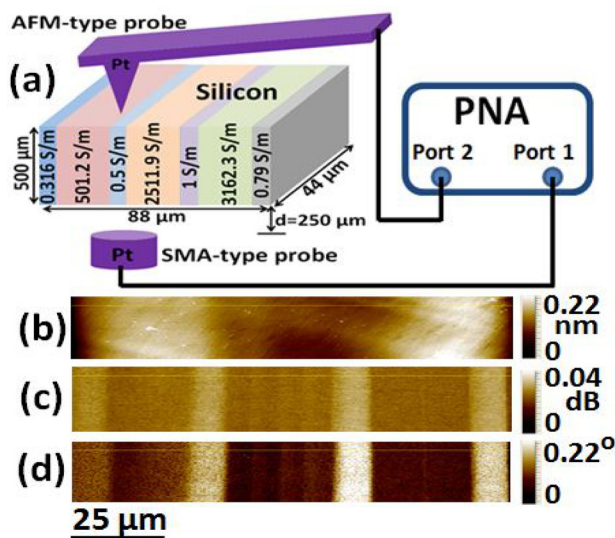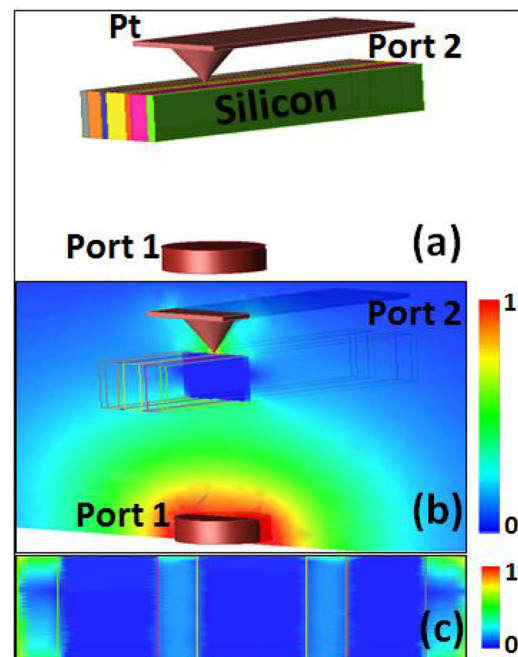

FIG. 1. (a) Schematics of a TM-SMM system showing the sample placed in-between the AFM and SMA probe. Experimentally determined (b) topography image, and (c) and (d) amplitude and phase contrast images of S_{21}, respectively, all obtained simultaneously from PNA feature of the TM-SMM.

FIG. 2. (a) 3D model of the TM-SMM, where ports 1 and 2 have been modeled as 50 Ω matched ports. (b) The normalized electric field profile when port 1 is the excitation port. (c) The normalized electric field distribution inside the sample (log scale).

For the dopant profiling sample used in this study, we compare in Figs. 3(a) and 3(b) the cross-sectional dependence of the variations of the amplitude, $\Delta\rho_{21}$, and phase, $\Delta\varphi_{21}$, obtained both from experiment and our 3D FEM simulations. We found good qualitative agreement between the measured and computationally determined profiles of $\Delta\rho_{21}$ and $\Delta\varphi_{21}$; however, there are large quantitative differences between the experimental results and those predicted by simulations. This finding suggests that losses and leakage contributions affect the experimental data, changing both the noise level and the radiation pattern. While loss effects can be readily included in the FEM simulations, their analysis is beyond the scope of this article as comprehensive experimental data are currently not available. In addition, in our simulations, we used a simplified structure for the SMA-type probe, which is markedly different from the antenna design used in the experiment. We believe though that adequate calibration and incorporation of resonant elements can further reduce the losses in the TM-SMM system and improve its sensitivity.

We also studied the effect of the conductivity of the bulk silicon substrate on the S-parameters by varying it from zero to 1000 S/m. We distinguish two main regimes,[15] illustrated in Fig. 4, with markedly different dependence of the S-parameters on the substrate conductivity. In the first case ($0 < \sigma_s \lesssim 100$ S/m), the substrate behaves like a dielectric, the S-parameters varying linearly with σ_s, while in the second regime (100 S/m to 1000 S/m) the substrate can be considered to be nearly metallic, the scattering parameters depending nonlinearly on σ_s. A transition region between the two regimes can be observed as a dip in the profiles of $\Delta\rho_{22}$ and $\Delta\varphi_{21}$. More specifically, in the first regime, both the amplitude and phase of the S-parameters depend almost linearly on σ_s, whereas in the second regime, this conductivity dependence becomes nonlinear. Importantly, Fig. 4 shows that the sensitivity of S_{22} and S_{21} parameters to variations in the conductivity of the silicon substrate is greater in the first
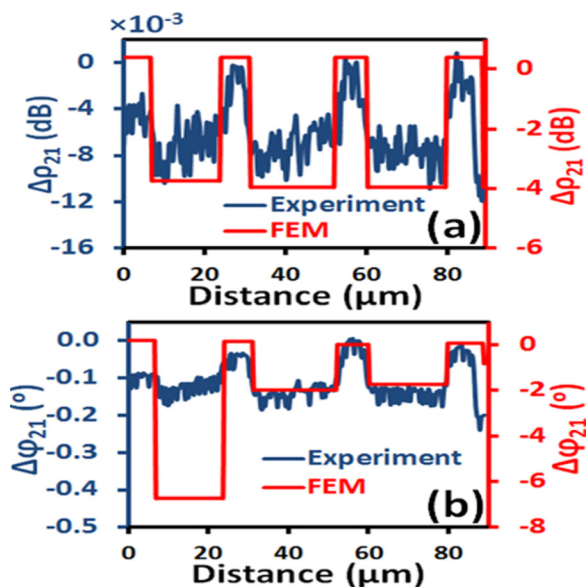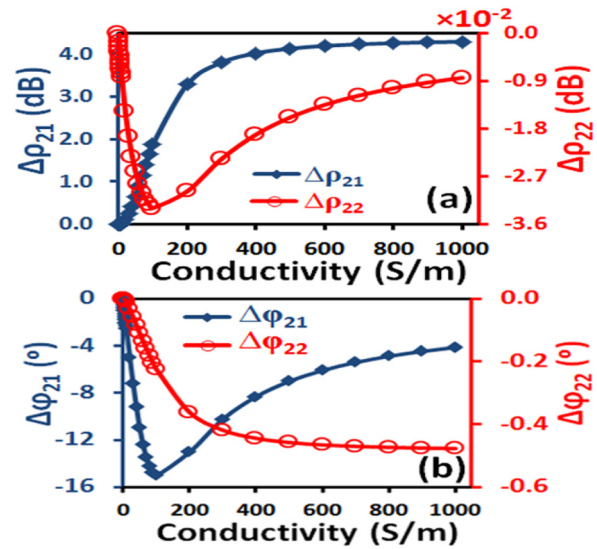

FIG. 4. (a) Variation of the amplitude and (b) phase of S-parameters vs. the conductivity of the silicon substrate. Circles and squares correspond to S_{22} and S_{21}, respectively.

(dielectric-like) regime than in the second (metallic-like) regime. These results indicate that the dopant density of the substrate in the sample plays a key role in determining the amplitude and phase of the scattering parameters and thus it should be accurately known.

In order to study the sensitivity of the S-parameters, we considered a sample configuration that can be readily fabricated and characterized [see Fig. 5(a)]. It comprises a relatively thick layer of substrate ($h_s = 300\ \mu$m, $\varepsilon_s = 12$, $\sigma_s = 4.1$ S/m) on top of which a disc, ($h_b = 200$ nm, $\varepsilon_b = 7$) is placed. The disc is buried underneath a covering circular plate of polymer ($\varepsilon_c = 2.4$) with thickness, h_c.

We first studied the effect of varying the depth, $h_d = h_c - h_b$, of subsurface constituents on the S-parameters. As seen in Fig. 5(b), $\Delta\rho_{21}$ ($\Delta\rho_{22}$) decreases (increases) nonlinearly with the depth h_d. Figure 5(c) shows that, by contrast, both $\Delta\varphi_{21}$ and $\Delta\varphi_{22}$ increase with the depth. We find that, on a linear scale, $\Delta\rho_{21}$ and $\Delta\varphi_{21}$ are at least twice as large as $\Delta\rho_{22}$ and $\Delta\varphi_{22}$, respectively. Also, Figs. 5(b) and 5(c) show that the sensitivity of the S-parameters to changes of the depth of subsurface constituents increases with the frequency.

We extended our investigation to the influence of the permittivity of the material ($h_c = 600$ nm) covering the subsurface constituent ($\varepsilon_b = 7$) of the sample, by varying it from $\varepsilon_c = 2$ to $\varepsilon_c = 16$. As shown in Figs. 5(d) and 5(e), both the amplitude and phase of the S-parameters vary nonlinearly with the permittivity of the covering plate. Importantly, we found that, on a linear scale, $\Delta\rho_{21}$ is twice as large as $\Delta\rho_{22}$, whereas $\Delta\varphi_{21}$ is more than 4× larger than $\Delta\varphi_{22}$. Moreover, we studied the effect of varying the permittivity of the subsurface constituent of the same sample on the system sensitivity, by varying the permittivity (from $\varepsilon_b = 2$ to $\varepsilon_b = 16$) of the subsurface disc ($h_b = 200$ nm) buried beneath a polymer plate ($\varepsilon_c = 2.4$, $h_c = 600$ nm). Similar to the previous case, we found that both the amplitude and phase of the S-parameters vary nonlinearly with the permittivity of the buried constituent. In this case, however, the sensitivity of $\Delta\varphi_{21}$ is

FIG. 3. Cross-sectional profile of (a) amplitude variations $\Delta\rho_{21}$ and (b) phase variations $\Delta\varphi_{21}$, obtained from experiment (blue line) and 3D FEM simulations (red line).
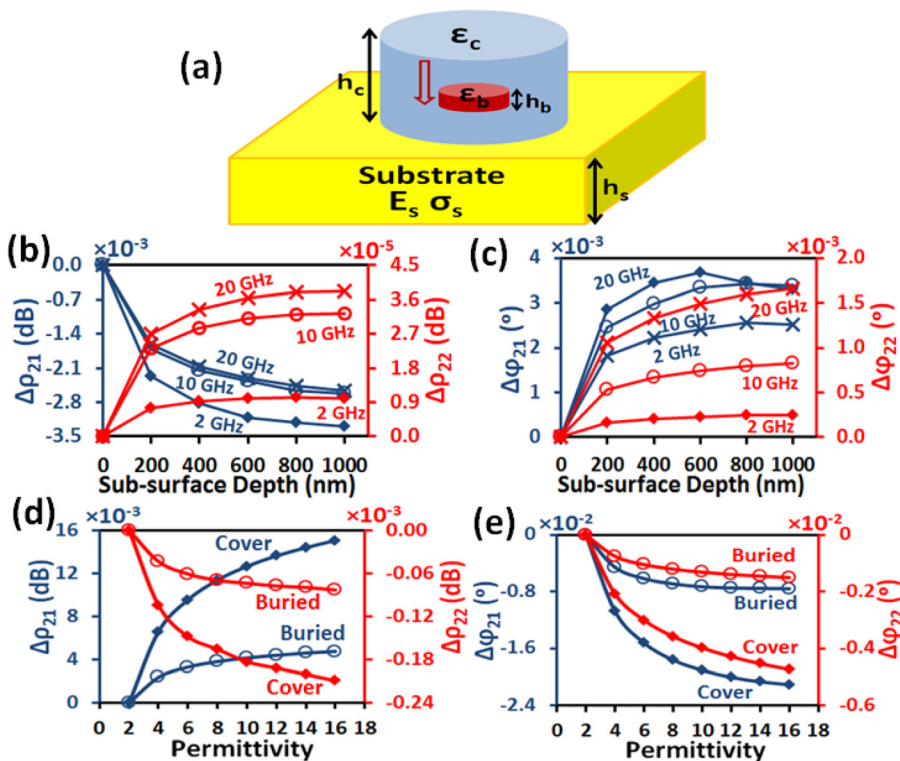
FIG. 5. (a) Schematics of the sample design. (b) and (c) Variation of the amplitude $\Delta\rho$ and phase $\Delta\varphi$, respectively, of the S_{21} (blue) and S_{22} (red) parameters with the subsurface depth d, computed for different frequencies. (d) and (e) Dependence of the amplitude and phase, respectively, of the S_{21} (blue) and S_{22} (red) parameters on the permittivity of the subsurface inclusion ε_b and covering material ε_c.

more than 6× larger than that of $\Delta\varphi_{22}$, whereas $\Delta\rho_{21}$ is twice as large as $\Delta\rho_{22}$. This shows that when operated in the transmission mode, the phase sensitivity is three time larger than the sensitivity of the signal amplitude, a key finding that suggests that the signal phase is the physical quantity to be used in TM-SMM imaging. Importantly, the actual values and variations of the S-parameters obtained from our computational investigations are well within the range of values that can be measured by the network analysis (PNA) feature of a SMM imaging system. These results suggest that the integration of TM-SMM to the current SMM technology can significantly improve the sensitivity of the system.

In conclusion, we have introduced and analyzed the TM-SMM, which is one of the latest improvements to the SMM technology. We used advanced 3D FEM computational techniques to study the effect of varying the conductivity of the substrate, the permittivity of buried constituents, as well as the permittivity of the covering material on the scattering parameters and found good qualitative agreement between our simulation results and the experimental data. Our analysis demonstrates that the TM-SMM provides improved sensitivity (from twofold to as much as six times increase) than that obtained in the currently used reflection mode SMM operation. In particular, we found the sensitivity of the phase of the S_{21} parameter to be three times larger than that of its magnitude. These conclusions have significant experimental implications as they provide valuable insights into the sensitivity of the TM-SMM and could guide the extension of SMM systems to advanced analysis tools with truly 3D imaging capability. This work can also identify operational aspects of SMM systems, which can be employed to further improve the system imaging efficiency.

[1]P. Alivisatos, Nat. Biotechnol. **22**, 47 (2004).
[2]X. Michalet, F. F. Pinaud, L. A. Bentolila, J. M. Tsay, S. Doose, J. J. Li, G. Sundaresan, A. M. Wu, S. S. Gambhir, and S. Weiss, Science **307**, 538 (2005).
[3]M. E. Davis, Z. Chen, and D. M. Shin, Nat. Rev. Drug Discovery **7**, 771 (2008).
[4]H-Y. Chen, M. K. F. Lo, G. Yang, H. G. Monbouquette, and Y. Yang, Nat. Nanotechnol. **3**, 543 (2008).
[5]M. M. van Schooneveld, A. Gloter, O. Stephan, L. F. Zagonel, R. Koole, A. Meijerink, W. J. M. Mulder, and F. M. F. de Groot, Nat. Nanotechnol. **5**, 538 (2010).
[6]E. Kymakis and G. A. J. Amaratunga, Appl. Phys. Lett. **80**, 112 (2002).
[7]B. T. Rosner and D. W. van der Weide, Rev. Sci. Instrum. **73**, 2505 (2002).
[8]D. M. Jones, J. R. Smith, W. T. S. Huck, and C. Alexander, Adv. Mater. **14**, 1130 (2002).
[9]D. Fotiadis, S. Scheuring, S. A. Muller, A. Engel, and D. J. Muller, Micron **33**, 385 (2002).
[10]L. Fumagalli, D. Esteban-Ferrer, A. Cuervo, J. S. Carrascosa, and G. Gomila, Nat. Mater. **11**, 808 (2012).
[11]S. Belaidi, P. Girard, and G. Leveque, J. Appl. Phys. **81**, 1023 (1997).
[12]C. Gao, T. Wei, F. Duewer, Y. L. Lu, and X. D. Xiang, Appl. Phys. Lett. **71**, 1872 (1997).
[13]M. Tabib-Azar and Y. Q. Wang, IEEE Trans. Microwave Theory Tech. **52**, 971 (2004).
[14]H. P. Huber, M. Moertelmaier, T. M. Wallis, C. J. Chiang, M. Hochleitner, A. Imtiaz, Y. J. Oh, K. Schilcher, M. Dieudonne, J. Smoliner, P. Hinterdorfer, S. J. Rosner, H. Tanbakuchi, P. Kabos, and F. Kienberger, Rev. Sci. Instrum. **81**, 113701 (2010).
[15]A. O. Oladipo, M. Kasper, S. Lavdas, G. Gramse, F. Kienberger, and N. C. Panoiu, Appl. Phys. Lett. **103**, 213106 (2013).
[16]M. Kasper, F. Kienberger, R. Feger, and A. Stelzer, *Agilent EMPro-SMM Application Note* (Agilent Technologies, Inc. 2013).